Lung functional imaging

Sam Bayat [1,2], Jim Wild[3,4] and Tilo Winkler [5]

[1]Department of Pulmonology and Physiology, CHU Grenoble Alpes, Grenoble, France. [2]Univ. Grenoble Alpes, STROBE Laboratory, INSERM UA07, Grenoble, France. [3]POLARIS, Imaging Group, Department of Infection Immunity and Cardiovascular Disease, University of Sheffield, Sheffield, UK. [4]Insigneo Institute, University of Sheffield, Sheffield, UK. [5]Department of Anesthesia, Critical Care and Pain Medicine, Massachusetts General Hospital and Harvard Medical School, Boston, MA, USA.

Corresponding author: Sam Bayat (sbayat@chu-grenoble.fr)

Shareable abstract (@ERSpublications)
Beyond pulmonary function testing, functional imaging provides deeper insights into regional heterogeneity and mechanisms of respiratory diseases with the potential for early detection and better phenotyping https://bit.ly/48MZNrB

Cite this article as: Bayat S, Wild J, Winkler T. Lung functional imaging. *Breathe* 2023; 19: 220272 [DOI: 10.1183/20734735.0272-2022].

Received: 2 May 2023
Accepted: 8 Oct 2023

Abstract

Pulmonary functional imaging modalities such as computed tomography, magnetic resonance imaging and nuclear imaging can quantitatively assess regional lung functional parameters and their distributions. These include ventilation, perfusion, gas exchange at the microvascular level and biomechanical properties, among other variables. This review describes the rationale, strengths and limitations of the various imaging modalities employed for lung functional imaging. It also aims to explain some of the most commonly measured parameters of regional lung function. A brief review of evidence on the role and utility of lung functional imaging in early diagnosis, accurate lung functional characterisation, disease phenotyping and advancing the understanding of disease mechanisms in major respiratory disorders is provided.

Introduction

Characteristic changes in lung function tests are a hallmark of many pulmonary diseases. However, regional changes in lung structure and function can precede detectable changes in global parameters particularly in the early stages of airway or parenchymal diseases. In virtually all lung diseases, local structural and functional alterations are heterogenous, while traditional lung function measurements can only provide global measurements. For example, small airways, which have been called the lung's "silent zone", contribute very little to the overall airflow resistance and local small airway disease can evolve long before it is detected by global pulmonary function tests, while it can be detected by imaging at an earlier stage [1].

Historically, we can trace the roots of pulmonary functional imaging back to 1960, when Dyson *et al.* [2] and West and Dollery [3] used a single coincidence detector pair, the precursor of modern positron emission tomography (PET), to investigate variations of regional perfusion and ventilation in the lungs. They identified a vertical profile, very similar to a gradient, in perfusion that contributed to developing the well-known physiological concept of West zones, which explains the effect of gravity on regional perfusion.

Modern pulmonary functional imaging uses various modalities, such as computed tomography (CT), magnetic resonance imaging (MRI) and nuclear imaging (single-photon emission computed tomography (SPECT) and PET), to assess the regional distribution of lung ventilation, perfusion, alveolar–capillary gas exchange, alveolar microstructure, biomechanical properties, and cellular or molecular processes such as inflammation or gene expression. The term "molecular imaging" is often used to refer to the latter. The various steps that are involved in acquiring a functional lung image are described in figure 1. The first step involves a quantitative measurement of a source of signal or contrast, which can be an exogenous contrast agent for CT or MRI, a pulse sequence relaxation weighting of the endogenous signal from the tissue and blood in the lungs in ^{1}H MRI, or a radionuclide tracer for SPECT or PET imaging. If this quantitative

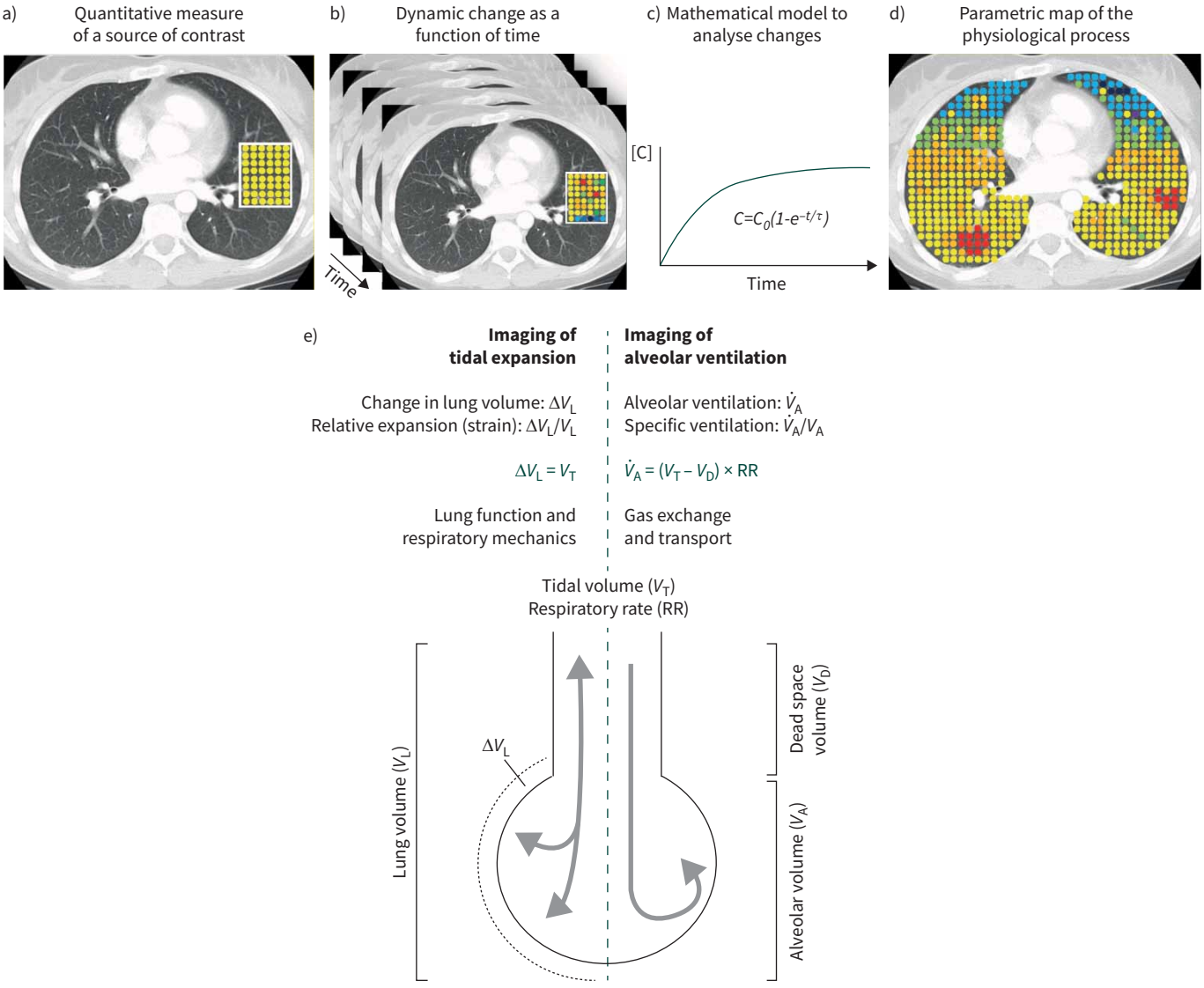

FIGURE 1 Successive steps involved in the acquisition and computation of a parametric map of a local functional parameter, such as lung ventilation measured by dual energy computed tomography imaging. a) A source of contrast is quantified within the image. b) Image acquisition is repeated over short periods of time. c) A mathematical model is usually used to fit the temporal dynamics of contrast as a function of time. d) The set of images is converted to a parametric map. e) Imaging of tidal expansion and alveolar ventilation assesses different lung function parameters. Changes in lung volume are related to the airflow at the airway opening, tidal volume, ventilation mechanics, and relative volume expansion, commonly referred to as lung strain. By contrast, alveolar ventilation is related to gas exchange and transport, such as oxygen and carbon dioxide.

measurement is repeated over short periods of time, then dynamic changes can be measured. Usually, a mathematical parametric model fit is used to extract the parameter of interest, which allows conversion of a set of images into a regional parametric map of the physiological process in question.

Besides detecting disease processes early on, functional imaging can also allow the precise description of the patient's lung functional phenotype. Such precise phenotyping is valuable in describing individual patient characteristics and disease trajectories, and in providing surrogates for clinical outcomes as imaging biomarkers for assessing new therapeutic interventions. These capabilities of functional imaging are integral parts of precision and personalised medicine [4]. Additionally, functional imaging provides a unique insight into disease processes and a better understanding of the mechanisms involved in airway and parenchymal diseases, whilst also providing unique regional insight into the signals obtained with global lung function tests.

The goal of this review is to describe the functional parameters that can be quantified by different imaging modalities, and to provide an overview of examples of their application in major lung diseases.

Regional lung functional parameters measured by imaging

Ventilation

Alveolar ventilation ($\dot{V}_A$; units: mL·min^{-1}) is the volume of fresh or tracer gas delivered to the alveolar space per unit time. Specific ventilation ($s\dot{V}$) is defined as the fraction of regional gas volume that is renewed by fresh gas per unit time, in other words: $\dot{V}_A/V_g$ (units: min^{-1}) where V_g is the end-expiratory gas volume within the considered region (table 1). It is a parameter that indicates how efficiently a given lung region is ventilated. Alternatively, $\dot{V}_A$ can be normalised to tissue mass, if that quantity is measured [5]. These definitions apply to dynamic image acquisition regimens incorporating time (figure 1). It is important to note that $s\dot{V}$ is not dependent on the volume of the considered region. For example, the $\dot{V}_A$ of an alveolus relative to its gas volume can be the same as for the lungs. Additionally, $\dot{V}_A$/volume distributions can visualise mismatches between regional ventilation and gas volume, the concept is equivalent to ventilation/perfusion ($\dot{V}/\dot{Q}$) distributions. Some imaging techniques rely on static end-inspiratory and end-expiratory images to measure a specific gas volume change ($s\Delta V_g$) or tidal expansion expressed per breath.

CT has been used to measure regional ventilation by imaging the kinetics of Xenon (Xe) gas washin or washout [6, 7]. Due to its high density, Xe enhances X-ray attenuation which can be quantified and allows measurement of the rate of washin or washout of a Xe–O_2 mixture, hence $s\dot{V}$. K-edge subtraction imaging uses two monochromatic X-ray beams produced with a synchrotron and material decomposition to directly quantify the distribution of Xe in the lung [8]. This imaging modality is free from beam hardening, and several times more sensitive and spatially resolved than standard CT; however, it is not available for clinical application due to the cost and scarcity of synchrotron sources.

Dual-energy CT (DECT) methods use two sets of images acquired with different X-ray photon energies (*e.g.* 80 and 140 kilo electron volt (keV)), obtained with various methods [9], to allow for a higher sensitivity to Xe than standard clinical CT. This technique also uses material decomposition, a method to extract element-specific contrast, with the caveat of beam hardening with polychromatic X-ray sources that complicates quantification. Nevertheless, DECT may allow simplified ventilation imaging with a single Xe gas mixture inhalation or to reduce the inhaled concentration to ∼30% in order to minimise anaesthetic side-effects if the gas is repeatedly inhaled [10]. The development of photon-counting spectral CT techniques may achieve a higher sensitivity allowing the use of Krypton, a less dense gas than Xe but without anaesthetic properties [10].

TABLE 1 Definition of functional imaging variables

Variable		Definition	Unit
Alveolar ventilation	$\dot{V}_A=\Delta V/t$	Volume of gas renewed per unit time in VOI	mL·min^{-1}
Specific ventilation	$s\dot{V}_A=\dot{V}_A/V_g$	Ventilation per unit gas volume in VOI	min^{-1}
Specific volume change	$s\Delta V_g=\Delta V_g/V_{g0}$ $s\Delta V_g=\Delta V_g/m_{tissue}$	Gas volume change per unit initial gas volume in VOI Gas volume change per unit tissue mass in VOI	dimensionless mL·g^{-1}
Ventilation defect percentage	VDP	Volume of lung with low hyperpolarised gas signal intensity, normalised to lung volume	dimensionless (%)
Perfusion	$\dot{Q}=\Delta V_B/t$	Volume of blood replaced per unit time in VOI	mL·min^{-1}, mL·100mL^{-1}·min$^{-1\#}$
Mean transit time	$MTT=V_B/\dot{Q}$	Average time it takes for blood to flow through the pulmonary vessels	s
Ventilation/perfusion ratio	$\dot{V}_A/\dot{Q}$	Ratio of ventilation to perfusion in VOI	dimensionless
Blood volume	V_B	Volume of blood in VOI	mL
Biomechanics			
Strain	$\epsilon=\Delta V_g/V_{g0}$	Gas volume change relative to initial gas volume in VOI, or: $J-1$	dimensionless
Elastance	$E=\Delta P_{rs}/\Delta V_g$	Pressure change required to induce gas volume change in VOI	hPa·mL^{-1}, cmH_2O·mL^{-1}
Jacobian	J	Determinant of the tissue deformation matrix between two different volumes	dimensionless

VOI: volume of interest. #: further normalised to tissue volume.

Instead of using an inhaled contrast gas, static three-dimensional (3D) lung CT images acquired at two different volumes (*e.g.* total lung capacity (TLC) and functional residual capacity (FRC) or residual volume (RV)) can be used to measure $s\Delta V_g$ [11], assuming that blood and tissue volume remains constant. This is based on measuring the local difference in attenuation, that reflects the change of the air content in a given voxel assuming the overall lung tissue and blood content remains unchanged. However, because the lung parenchyma moves between the two inflation states, elastic image coregistration algorithms are required to warp one image to match the other (figure 2). Similar approaches have been proposed to quantify air trapping (> −950 Hounsfield units (HU) on inspiration but < −856 HU on expiration) and distinguish functional small airway disease (PRM^{fSAD}) from emphysema (PRM^{Emph}) (both < −950 HU on inspiration and < −856 HU on expiration) represented as a "parametric response map" (PRM) [12].

Hyperpolarised gas MRI provides another means of assessing regional lung ventilation distribution (figure 3). This method involves imaging small, inhaled volumes of inert gases whose nuclear magnetisation has been massively enhanced by laser optical pumping to give a strong direct signal from gas in the lungs. Hyperpolarised helium-3 (^{3}He) was initially tested most extensively due to its intrinsically stronger signal-to-noise ratio [13]; however, due to scarcity and cost of ^{3}He, ^{129}Xe is now being increasingly used for this purpose. In addition, Xe is soluble so can be used to measure regional gas exchange (discussed later). Ventilation imaging is usually performed at breath hold after inhaling between 300 and 1000 mL of the hyperpolarised gas (or a set percentage of TLC), starting at FRC. Regional ventilation has been assessed using a scoring system or quantitatively by measuring the volume of poorly ventilated regions, expressed as a percentage of lung volume, estimated from coregistered proton (^{1}H) MRI

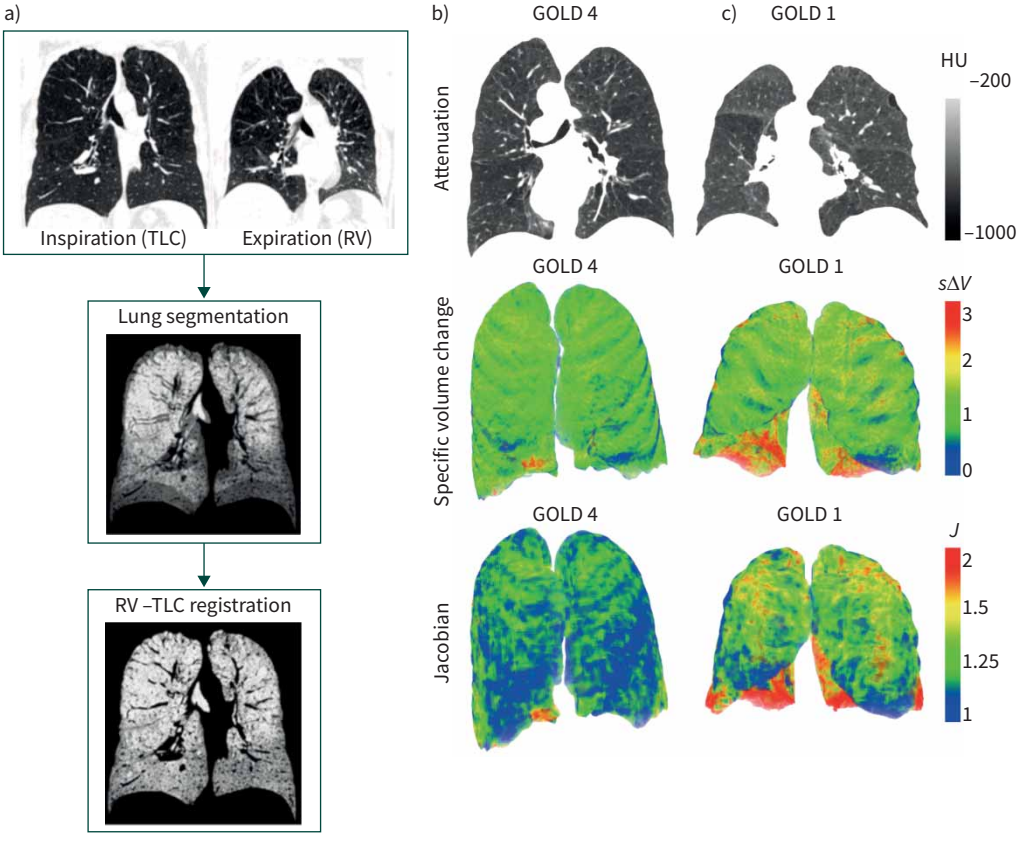

FIGURE 2 a) Registration-based computation of local volume change and deformation. Computed tomography images acquired at total lung capacity (TLC) and residual volume (RV) are first segmented. The segmented images are superimposed using rigid image registration. Greyscale inverted to highlight the deformation between the two states. Non-rigid registration algorithms are then applied to warp the RV to fit the TLC image. b, c) lung image attenuation, specific volume change ($s\Delta V$) and Jacobian determinant (J) in b) a Global Initiative for Chronic Obstructive Lung Disease (GOLD) stage 4 and c) a stage 1 COPD patient. HU: Hounsfield units.

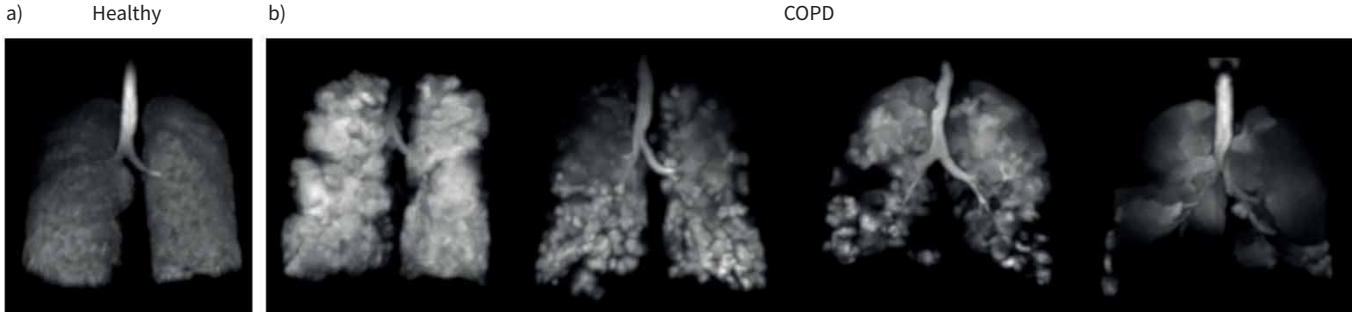

FIGURE 3 Sample hyperpolarised helium-3 (^{3}He) images in a) a normal subject and b) patients with COPD. Note the inhomogeneous distribution of the inhaled ^{3}He gas in the subjects with COPD.

images [14], termed ventilation defect percentage (VDP) [15]. These metrics of lung ventilation have been shown to be extremely sensitive to early obstructive lung disease in cystic fibrosis (CF) and smokers where spirometry remains normal. These metrics have been used to assess regional changes in lung ventilation in response to treatments ranging from chest physiotherapy to bronchodilators and cystic fibrosis transmembrane conductance regulator (CFTR) modulators in CF. Images are typically acquired in 3D or multiple two-dimensional slices and can be acquired at different inflation levels to assess partial obstruction/air trapping [16]. Alternatively, images can be acquired dynamically during a single breath [17, 18] or over a multiple breath washout [16] to map parameters such as $s\dot{V}$. An alternative to hyperpolarised gas MRI for mapping lung ventilation with inhaled tracer gas MRI uses fluorine-19 (^{19}F) perfluorinated gases [19], which can also be imaged dynamically as well as at breath hold.

Alternatively, oxygen-enhanced MRI can be used to measure ventilation distribution during free breathing. This technique is based on the decrease in T1 relaxation time of the water molecules in parenchymal tissue and blood in the lungs in ventilated regions, where the weakly paramagnetic molecular O_2 is dissolved [20]. The rate of this signal change allows measurement of $s\dot{V}$ [21].

A major advantage of MRI is the absence of ionising radiation exposure, even though very low radiation dose CT imaging with acceptable image quality is increasingly performed. As lung tissue contains a large fraction of air, there is inherently a low proton density, and the large number of air–tissue interfaces produce local magnetic field gradients that act to dephase the magnetic resonance (MR) signal (shorten T2*). These factors lower the spatial resolution and signal-to-noise ratio of proton imaging (table 2) [13]; however, MRI of the lung parenchyma using ultrashort echo time sequences is now providing clinically useful structural lung images [22]. Coregistration of short echo time of static ^{1}H MRI acquired at different volumes has been used to measure regional lung volume changes, which correlated well with ^{3}He MRI ventilation images [23]. Alternatively, Fourier decomposition of free-breathing ^{1}H MRI images can be used to assess the signal change due to ventilation and perfusion.

PET, SPECT and planar scintigraphy require use of radioisotopes suitable for the imaging modality (*e.g.* using nitrogen-13 (^{13}N) for PET). Additionally, the radioisotope must be part of a tracer with physical and chemical properties that allow the assessment of ventilation. An ideal tracer would be a chemically inert and insoluble gas that remains unchanged and in the gas phase. Excellent tracers with such properties that have been used for PET are neon-19 (^{19}Ne) and ^{13}N-N_2 nitrogen gas. Note that there are varying notations for N_2 containing ^{13}N, for example, ^{13}NN emphasises that the isotope production favoured N_2 molecules with one ^{13}N and one stable nitrogen isotope from the air. By contrast, tracers used for SPECT and scintigraphy ventilation imaging are 99-metastable-technetium (^{99m}Tc)-labelled aerosols (*e.g.* ^{99m}Tc diethylene triamine pentaacetic acid (DTPA) or Technegas) deposited in the alveoli, or the gaseous xenon-133 (^{133}Xe) or 81-metastable-krypton (^{81m}Kr). The typical clinical use of SPECT and scintigraphy ventilation imaging is as part of $\dot{V}/\dot{Q}$ scans for the evaluation of pulmonary embolism [24].

Pulmonary ^{13}NN PET imaging was pioneered at the Hammersmith Hospital (London, UK) using a continuous infusion technique to assess regional $\dot{V}/\dot{Q}$ ratios [25]. The ^{13}NN-bolus injection method was developed at Massachusetts General Hospital (Boston, MA, USA) to assess ventilation and perfusion [26]. Both methods deliver the tracer by perfusion and measure the elimination by regional ventilation. But the continuous-infusion method measures the regional differences in ^{13}N delivery and elimination at

TABLE 2 Characteristics of the different imaging modalities for functional imaging

Modality	Spatial resolution	Length	Cost	Availability	Advantages	Limitations
CT	Highest	Seconds	Low	Available	Resolves detailed parenchymal morphology	Ionising radiation Allergy to iodine contrast in some subjects
DECT	Highest	Seconds	Low	Less available	Resolves detailed parenchymal morphology; contrast-material specific imaging	Ionising radiation Allergy to iodine contrast in some subjects
HP gas MRI	High	Seconds to minutes	Non-contrast: low HP gas: high	Non-contrast: available HP gas: less available	No ionising radiation Versatile: different pulse sequences allow resolving various sources of contrast	Parenchymal signal-to-noise ratio lower than CT No metal implants Concerns with gadolinium (Gd) contrast brain retention Hyperpolarisation hardware intensive
SPECT	Low	Minutes	Low	Available	Very high contrast sensitivity	Ionising radiation Does not resolve lung morphology
PET	Moderate	Minutes	High	Less available	Very high contrast sensitivity	Ionising radiation

CT: computed tomography; DECT: dual-energy CT; HP: hyperpolarised; MRI: magnetic resonance imaging; SPECT: single-photon emission CT; PET: positron emission tomography.

equilibrium conditions, while the ^{13}NN-bolus injection method analyses the tracer kinetics using dynamic PET scans. The inhalation of ^{13}NN has also been used for ventilation imaging [27].

The advanced analysis of the washout kinetics of the ^{13}NN-bolus injection method uses four models, including single-compartment washout, two-compartment washout, gas trapping, and a combination of a gas trapping and a washout compartment (figure 4). The time constant of the washout is proportional to the $s\dot{V}$. A separate assessment of alveolar volume (*e.g.* by CT imaging) allows the conversion to $\dot{V}_A$. Combined with a perfusion assessment, $\dot{V}/\dot{Q}$ distributions based on this method have accurately predicted arterial blood gases under highly heterogeneous conditions in the lungs validating the ^{13}NN-bolus injection method [28].

In summary, direct quantification of $\dot{V}_A$ requires measuring the renewal of gas per unit time (table 1, figure 1), usually using an inert tracer gas. In CT imaging, the change in X-ray attenuation between two lung inflation states is an indirect measure of the change in gas volume. Measuring gas volume change based on attenuation change assumes constant tissue and blood volume within the lung volume of interest (VOI). Regardless of the imaging modality, a calculated volume change can be expressed in absolute terms (ΔV_g; units: mL) or relative to the initial gas or tissue volume ($s\Delta V_g$).

Perfusion

Perfusion ($\dot{Q}$; units: mL·min^{-1}) is the volume of blood delivered to a given region per unit time. $\dot{Q}$ is sometimes further normalised to tissue volume and expressed as mL·100mL^{-1}·min^{-1}. In CT, it can be measured using dynamic imaging during iodine or gadolinium contrast injection and indicator dilution theory [29], based on the first pass kinetics of the contrast material. $\dot{Q}$ is calculated as the ratio of peak parenchymal enhancement, based on the attenuation *versus* time curve of a given parenchymal voxel, to the area under the time–attenuation curve of a reference pulmonary artery [30]. Lung perfused blood volume (V_B or PBV) is obtained by the ratio of the late-phase or steady-state parenchymal contrast element mass computed by material decomposition, to the concentration within a main pulmonary arterial lumen: V_B=q/[C]. This method also allows measuring the contrast mean transit time (MTT) as: $V_B/\dot{Q}$. Pulmonary V_B may alternatively be assessed during slow contrast injection or at steady concentration contrast infusion. Previous studies with DECT have shown that V_B and $\dot{Q}$ are correlated, which is plausible if the blood volume is representative of the vessel diameter that affects its resistance [30]. However, it remains unclear if the quantitative relationship is fixed and always linear. For example, local obstructions, local hypoxic vasoconstriction, which is severely blunted in acute lung injury [31], and similar mechanisms could act like a valve inserted in a tube affecting the flow without a substantial effect on the upstream volume.

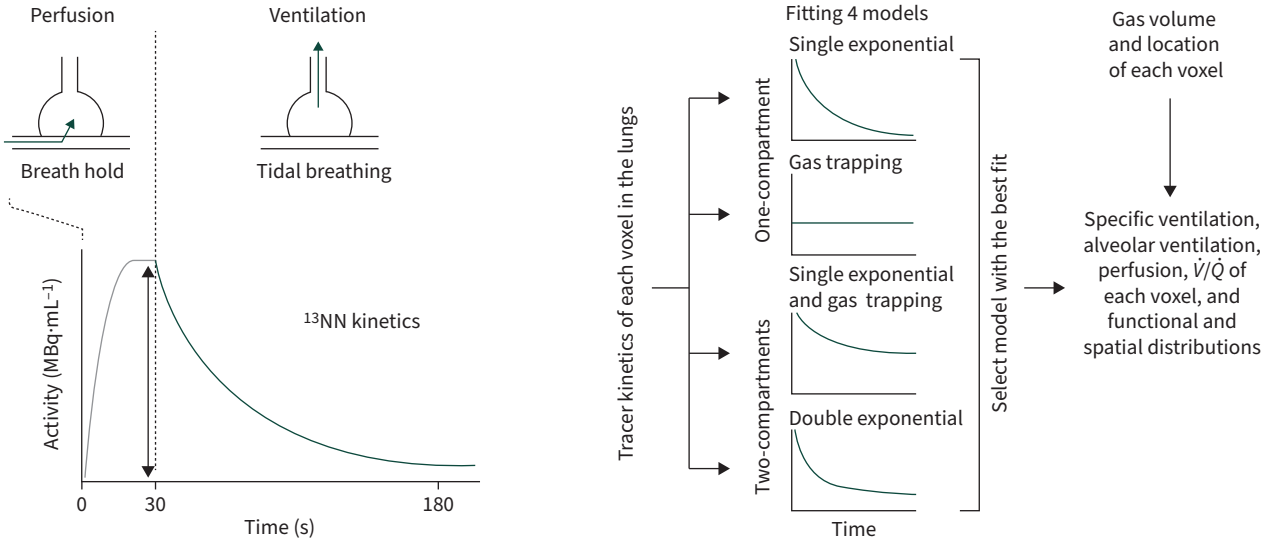

FIGURE 4 Schematic of the positron emission tomography ^{13}NN-saline bolus-injection method for assessment of regional perfusion ($\dot{Q}$) and ventilation ($\dot{V}$). The ^{13}NN tracer reaching the alveoli is proportional to perfusion and diffuses due to its low solubility from the blood into the alveoli. The tracer kinetics during washout using four models allows the assessment of sub-resolution functional compartments. Combining the parameters of ^{13}NN kinetics with gas fraction measurements from corresponding computed tomography images yields a substantial number of lung function parameters and their regional differences. ^{13}NN: N_2 containing ^{13}N; units: MBq.

Dynamic contrast-enhanced perfusion MRI is based on imaging the passage of an injected bolus of a T1-contrast agent from the right heart, through the pulmonary vasculature to the left heart using time-resolved imaging. MR angiography also allows assessment of the systemic bronchial circulation. The T1 signal enhancement *versus* time course is converted to a calculated concentration–time course in a given parenchymal voxel, which gives the parenchymal function. Following a brief delay corresponding to the transit of contrast through the vasculature, the signal sharply rises with the arrival of contrast, then declines to lower values as the contrast recirculates. The first pass portion of this curve can be fit by a gamma variate function both in the parenchymal region of interest, and in a reference pulmonary artery. $\dot{Q}$, V_B and MTT are then obtained from these curves, based on indicator dilution theory [32]. A limitation of contrast-enhanced MRI is the concern about the retention of gadolinium within the brain, with uncertainties regarding its long-term effects (table 2) [33].

Non-contrast MRI techniques have also been developed for perfusion imaging, mainly as investigative methods. One such approach is arterial spin labelling. Here, two ECG-gated images are acquired a few seconds apart, where the ^{1}H signal within the blood is modified by radiofrequency pulses between the two images, so that their subtraction yields a parametric map of lung perfusion [34]. This approach has been used to study lung perfusion in a variety of physiological conditions [35]. Another non-contrast approach is the Fourier decomposition technique. This free-breathing method is based on separating the changes in ^{1}H MR signal due to breathing and blood flow, which allows relative assessment of ventilation and perfusion [36]. For characterisation of blood flow in the major pulmonary arteries and veins four-dimensional velocity flow mapping can be performed providing time-resolved maps of blood flow in the main pulmonary vessels [37] and information on the cardiopulmonary vascular pulse wave.

SPECT and scintigraphy utilise ^{99m}Tc-labelled macroaggregated albumin. Most of the injected microspheres are trapped during their first pass in pulmonary capillaries [38], and their relative distribution is proportional to regional blood flow. Such scans are part of $\dot{V}/\dot{Q}$ scans for assessing pulmonary embolism.

PET ^{13}NN-saline bolus-injection for perfusion imaging can assess mean-normalised regional perfusion and differentiate up to two sub-resolution compartments per voxel using washout kinetics (figure 4). The $\dot{V}/\dot{Q}$ distributions resulting from the assessment of ventilation and perfusion accurately predicted arterial blood gases validating the method [28, 39]. Alternatively, the tracer distribution at the end of an initial breath hold is proportional to the relative distribution of perfusion (figure 4). Importantly, accounting for imaging noise (the random measurement errors of the individual voxels) in PET scans allows assessment of perfusion heterogeneity [40], which can be significantly different in patients with lung diseases compared

with controls [41, 42]. Additionally, it should be noted that ^{13}NN methods measure pulmonary perfusion at the capillary level because they assess the tracer transfer from the capillaries into the alveoli.

The PET ^{13}NN continuous-infusion technique requires an additional ventilation scan to derive regional perfusion [25]. A ^{15}O-H_2O method also requires two scans for a model-based assessment of regional perfusion [43]. Clinical investigations typically use Gallium-68 (^{68}Ga)-labelled macroaggregated albumin to assess pulmonary perfusion.

$\dot{V}/\dot{Q}$ ratio

The $\dot{V}/\dot{Q}$ ratio is a fundamental parameter of gas exchange and $\dot{V}/\dot{Q}$ distributions characterise the contributions of different functional lung units, including pulmonary shunt as the lowest $\dot{V}/\dot{Q}$ ratio and alveolar dead space as the highest. Most of the published $\dot{V}/\dot{Q}$ distributions were measured using the multiple inert gas elimination technique (MIGET), *e.g.* [44]. In contrast to the overall characterisation of the lungs obtained using MIGET, PET, MRI and SPECT imaging allow regional assessments of $\dot{V}/\dot{Q}$ ratios and associated gas exchange parameters [24, 28, 45, 46]. For example, $\dot{V}/\dot{Q}$ imaging has provided insights into highly heterogeneous regional variations in ventilation and perfusion that can explain changes in arterial blood gases [28], estimates of alveolar O_2 and CO_2 partial pressures in ventilation defects (VDefs) during bronchoconstriction in asthma [47, 48], regional O_2 and CO_2 transfer in asthma [49], the spatial distribution of alveolar dead space and its effects on gas exchange in early acute respiratory distress syndrome [50], and the effects of nitric oxide (NO) inhalation on regional perfusion and $\dot{V}/\dot{Q}$ in pulmonary arterial hypertension [51]. Clinically, SPECT $\dot{V}/\dot{Q}$ scans are, for example, used for regional examination in pulmonary embolism.

An important distinction between MIGET and $\dot{V}/\dot{Q}$ imaging is that the MIGET method measures six inert gases and uses a smoothing function to estimate $\dot{V}/\dot{Q}$ distributions with 50 data points, while imaging-based $\dot{V}/\dot{Q}$ distributions are comparable to histograms of the voxel data inside the lung mask [51]. The heterogeneity of $\dot{V}/\dot{Q}$ distributions can be characterised as the standard deviations of the perfusion-weighted and ventilation-weighted natural logarithm of the $\dot{V}/\dot{Q}$ distribution, typically referred to as log $_{SD}$ $\dot{Q}$ and log $_{SD}$ $\dot{V}$, respectively [51–53].

Exchange at the capillary–alveolar barrier

Dissolved phase xenon MRI provides a means to assess regional gas exchange from the alveolus, through the interstitial tissue (membrane) and into the red blood cells (RBCs) in the capillaries. Xenon is soluble in tissues and RBCs, and the ^{129}Xe signal has a unique spectroscopic resonant frequency that depends upon the compartment and can thus be used to image gas transfer and membrane diffusion. Time resolved spectroscopic studies of membrane diffusion can be used to estimate membrane thickness [54, 55]. With spectroscopic imaging methods, maps of the signals in the gas, membrane and RBC compartments can be computed that provide regional information on gas exchange [56], which has been shown to be sensitive to disease progression in interstitial lung diseases [57, 58] and to disease severity in post-COVID-19 lung disease [59].

PET imaging of ^{68}Ga-transferrin has been used to assess the pulmonary transcapillary escape rate (PTCER) and has shown that PTCER is a sensitive but nonspecific index [60]. Alternatively, ^{15}O-H_2O can assess the regional distribution of lung water concentration [31].

Biomechanics

Strain is defined by the relative change in gas volume, mainly as a result of ventilation. It is a dimensionless parameter and expressed as the change in volume (ΔV_g) relative to the reference volume which may be RV, FRC or end-expiratory volume: $\Delta V_g/V_{g0}$. The volume with reference to which strain is measured is currently not standardised and should be systematically reported. Strain is identical to $s\Delta V_g$ (see the section entitled Ventilation). However, it is important to distinguish this metric from $s\dot{V}$, as illustrated in figure 2. The local lung stiffness or elastance is given by the pressure change (ΔP_{rs}) required to induce a given ΔV_g, or: $\Delta P_{rs}/\Delta V_g$ under conditions where regional alveolar pressures are fully equilibrated. Non-rigid coregistration of CT images acquired at two different lung volumes allows mapping the local lung strain based on the 3D transformation matrix between the two volumes. The determinant of this matrix is termed the Jacobian determinant or Jacobian. The Jacobian is a biomechanical metric that informs on the local lung deformation [61]. A Jacobian determinant value >1 indicates local expansion whereas a value <1 indicates local contraction. However, it should be noted that elastic registration algorithms have limitations in their accuracy and that Jacobians are estimates.

X-ray imaging with a synchrotron source allows imaging of parenchymal strain at a resolution of a few micrometres in small animals [62]. Imaging local lung elastance, however, requires knowledge of the pressure within the imaged airspaces at any given volume (table 1). This is feasible only in static conditions, reasonably assuming an equal pressure field within communicating airspaces at pressure equilibrium. However, during tidal breathing the local pressures within the airspaces cannot be directly measured.

Elastography uses shear wave propagation and the phase of the MRI signal to measure local lung deformation and estimate elastance, assuming a uniform pressure field. MR elastography has been applied in pilot studies in lungs in patients with interstitial lung disease to measure parenchymal stiffness [63].

Functional imaging of major pulmonary diseases

COPD

COPD is a heterogenous disorder with different phenotypes and progression. This disorder is characterised by varying degrees of small airway disease and emphysema, and is sometimes associated with fibrosis or pathological vascular structure [64]. There are very limited disease-modifying therapeutic options, in part because therapeutic advances are impeded by the difficulty in identifying subpopulations at risk of accelerated lung function decline [65]. There is an increasing focus on early detection and deep phenotyping of at-risk subjects and those with early COPD, in order for therapeutic intervention to prevent progression to emphysema. The COPDGene follow-up data have shown that PRM^{fSAD} at baseline is associated with subsequent forced expiratory volume in 1 s (FEV_1) decline [66] and emphysema development [67], suggesting it can serve as a surrogate imaging biomarker. CT registration-based regional *sV* change ($s\Delta V_g$) and Jacobian are associated not only with lung function, but also with symptoms, gas exchange and exercise capacity [68]. CT-based perfusion imaging has shown an increased $\dot{Q}$ heterogeneity in subjects with apical centrilobular emphysema, suggesting that reduced $\dot{Q}$ to regions with smoking-associated inflammation may be a causal factor in emphysema [69]. Regional lung ventilation has been assessed with Xe-enhanced DECT in subjects with COPD revealing reduced ventilation and trapping in regions with low attenuation due to emphysema [70].

Hyperpolarised gas ventilation MRI provides information on early obstructive lung disease (ventilation heterogeneity) in smokers before changes in airflow are detected with spirometry [14]. By measuring the Brownian diffusion coefficient early changes in alveolar dimensions related to subclinical emphysema can also be measured [71, 72]. In diagnosed COPD patients, hyperpolarised gas ventilation MRI can predict clinical exacerbation frequency in patients with mild–moderate severity. When ventilation MRI is combined with diffusion coefficient measurements of alveolar emphysema, the imaging can provide insight into emphysematous *versus* obstructive phenotypes [73]. Time-resolved imaging of delayed ventilation can also be used to assess collateral ventilation pathways across lung fissures [74] and has been used clinically to plan lung volume reduction surgery and endobronchial valve placement. Dissolved xenon MRI has also been used to understand mechanisms of gas transfer in patients with COPD [75].

COPD also affects the pulmonary vasculature causing significant changes in regional perfusion that may be an early indicator of the disease [41]. Furthermore, the association between COPD and HIV is poorly understood, but a recent PET imaging study found that HIV infection contributes to pulmonary perfusion abnormalities similar to those in smokers [76]. When ventilation MRI is combined with perfusion MRI, mechanisms of $\dot{V}/\dot{Q}$ matching in response to new therapies for COPD can be assessed [77, 78].

Asthma

Morphological CT imaging has allowed characterisation of airway remodelling, showing that increased airway wall thickness [79], but also obliteration by mucus plugging [80] is associated with disease severity and reduced lung function. Besides structural remodelling, airway distensibility and constriction has been studied with CT imaging in asthmatic subjects and has shown stiffer airways, inhomogeneous constriction [81, 82], and a greater propensity for airway closure [83]. These findings have suggested that an increased baseline airway wall thickness due to inflammation and remodelling in asthma patients promotes airway narrowing.

Ventilation distribution is known to be inhomogeneous in asthma patients based on inert gas washout even in the absence of symptoms or spirometric evidence of airway obstruction [84]. This feature of asthma was initially revealed by scintigraphy using radioactive ^{133}Xe [85]. Later SPECT studies with ^{99m}Tc-labelled carbon particles showed that the extent of VDefs after methacholine challenge is determined by small airway disease [86].

A fundamental contribution of functional imaging studies to the understanding of asthma is that they revealed the emergence of VDefs during bronchoconstriction (figure 5), leading to the development of a computational model that could explain the regional clustering of severe airway constriction. It demonstrated that it is an emergent phenomenon beyond a tipping point in airway narrowing [87–89]. The primary feedback among airways leading to VDefs can be explained using, for simplicity, a single airway bifurcation. Lower airflow in one daughter airway results in lower expansion of the tissue surrounding the airway, lowering the parenchymal tethering forces, increasing smooth muscle constriction, and increasing airway resistance. In contrast, the higher airflow in the other daughter airway results in higher regional tethering forces preventing further constriction.

CT imaging of airway wall area and other imaging-derived parameters has recently shown that they are epidemiological predictors of the rate of future exacerbations and lung function decline in severe asthma [90]. The far-reaching implications of these findings are that airway remodelling shifts the tipping point for the emergence of VDefs during an asthma attack or exacerbation, increasing the sensitivity to stimuli [89].

PET imaging has shown that aerosols inhaled during bronchoconstriction are deposited in airways of ventilated regions outside of VDefs, which has implications for the efficiency of bronchodilator delivery [91].

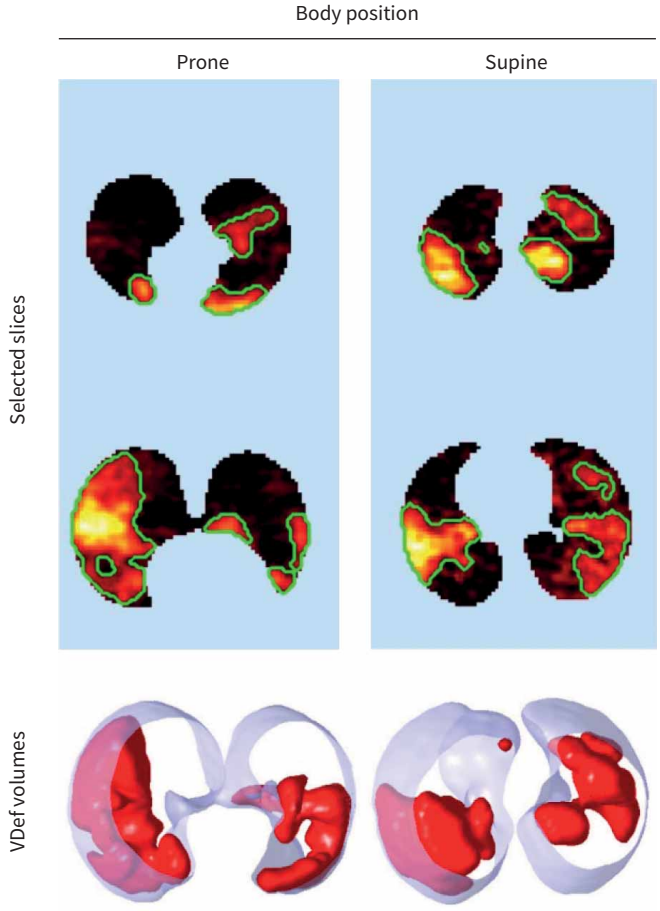

FIGURE 5 Example of positron emission tomography imaging of ventilation defects (VDefs) during bronchoconstriction in asthma using ^{13}NN. The severe airway constriction or closure of airways within VDefs results in the retention of the ^{13}NN, delivered by perfusion, inside VDefs, which are affected by body position. The selected slices using a "hot" colour scale show the magnitude of the tracer activity from low (black) to high (white). The green outlines illustrate the identified boundaries of VDefs visualised in three-dimensional renderings as VDef volumes inside the lungs (transparent blue). Images are from the same subject studied on two different days after receiving the methacholine challenge in the prone position on both occasions. Note the tendency of the VDefs location to be in a dependent part of the lungs suggesting an effect of regional parenchymal forces in contrast to aerosol deposition during prone inhalation. Reproduced from [135] with permission. ^{13}NN: N_2 containing ^{13}N.

Also, it has been demonstrated that bronchodilator inhalation can increase peak expiratory flow (PEF) without changing VDefs, which suggests an increase in PEF due to the dilation of airways outside of VDefs [92].

Perfusion inside VDefs is decreased, which could be expected, due to severely impaired regional ventilation causing hypoxic vasoconstriction [93]. Surprisingly, however, perfusion inside VDefs was lower than hypoxic and hypercapnic vasoconstriction predicted, suggesting that another mechanism contributes to the change [47, 48].

Hyperpolarised gas ventilation MRI has provided detailed insight into disease severity in adults and children [94], and into the regional response of the lungs to bronchodilators [95], novel biologic therapies [96] and bronchial thermoplasty [97]. Ventilation patterns from hyperpolarised gas ventilation MRI have been coupled to CT airway measurements to help phenotype small and large airways disease in asthma [98].

Xe-enhanced DECT imaging has also been used to study ventilation inhomogeneity and the presence of VDefs with comparison to spirometry [99].

It is becoming increasingly apparent that asthma is associated with heterogenous changes inside the lungs, where accurate phenotyping of patients and assessments of regional changes towards personalised treatment strategies is crucial. Both structural imaging of the airways and parenchyma, and ventilation imaging can provide useful means of accurate functional characterisation and provide outcome measures for the developing disease-modifying drugs.

Interstitial lung diseases

High-resolution CT plays a major role in the detection and follow-up of lung fibrosis. The individual progression of fibrosis is highly variable among patients [100]. The goal of antifibrotic drug therapy is to slow down the progression of the disease. In this context, the early identification of patients with a faster rate of disease progression is important for the optimisation of individual treatment. Functional imaging techniques have shown promise in the early identification and characterisation of lung fibrosis. DECT registration-based regional volume change and blood volume measured by late parenchymal contrast enhancement were both found to be associated with later decline in lung volume [101], providing potential biomarkers for fibrosis progression. Image registration has also been applied to match ^{1}H MRI images acquired upon inspiration and expiration to assess the local deformation based on the Jacobian. Using this approach, it was shown that subjects with scleroderma and lung fibrosis had a reduced deformation in dorsal regions of the lung bases, unlike normal controls or those with scleroderma but without fibrosis, although there was no added value beyond high-resolution CT for identifying fibrosis [102].

Hyperpolarised ^{129}Xe MRI has allowed mapping of the barrier thickening as well the reduced RBC transfer in patients with idiopathic pulmonary fibrosis (IPF) [103]. In addition, ^{129}Xe MRI has shown that RBC transfer decreases over a relatively short time interval of 1 year, while neither carbon monoxide diffusion capacity (D_{LCO}) nor forced vital capacity changes significantly, suggesting that this metric may be sensitive to disease progression [57]. Perfusion MRI has been used to assess microvascular changes in blood volume and lung transit time in IPF [104, 105].

Fluorine-18 2-fluoro-2-deoxy-D-glucose (^{18}F-FDG) PET imaging is used in lungs without cancer to assess regional metabolic activity associated with inflammation [106]. In interstitial lung disease, ^{18}F-FDG uptake parameters were correlated with baseline quality of life but were not predictors for the subsequent change in quality of life over 4 years [107]. Also, ^{18}F-FDG PET imaging has shown significant differences between rapid progression in interstitial lung disease and non-rapid progression [108].

Cystic fibrosis

CF is the most common genetic disorder causing premature death in the Caucasian population [109]. CF lung disease manifests in early childhood and is characterised by chronic bacterial infection and inflammation with episodic exacerbations leading to progressive bronchiectasis and lung function decline [110]. Chest CT is the gold standard for morphological characterisation of CF lung disease and the detection of bronchiectasis, air trapping and mucus plugging, with scoring systems that allow the assessment of disease progression [111]. However, radiation dose is a concern with repeated CT examination, particularly in young children who are more sensitive to radiation-induced malignancy [13]. CT ventilation or perfusion imaging are therefore scarce in this population. Both T1- and T2-weighted proton MRI is routinely used for the morphological follow-up of subjects with CF. A number of studies with hyperpolarised gas MRI have assessed VDP in subjects with CF. These have shown that hyperpolarised ^{3}He MRI is more sensitive

than spirometry, CT or lung clearance index (LCI) in detecting early lung disease in children with CF [112, 113], albeit in a small number of subjects. ^{3}He MRI was also able to detect the effect of therapy with CFTR modulators [114].

Dynamic contrast-enhanced MRI has previously been used to assess perfusion abnormalities in children and adults with CF, and showed a good correlation with multiple breath washout LCI [115]. Contrast-enhanced MRI is also able to detect exacerbations and recovery after antibiotic therapy, although concerns with gadolinium contrast retention in the brain limit its routine clinical use. More recently, Fourier decomposition approaches have been used for ventilation and perfusion imaging in children with CF. Relative fractional ventilation and relative perfusion showed strong correlations with LCI [116], and appeared promising for non-contrast monitoring of functional impairment in this population. The registration of breath hold inspiratory and expiratory MRI images allows measurement of the local change in ^{1}H signal which has been used to infer the local volume change in subjects with CF. This approach has the advantage of not requiring any tracer gas inhalation, correlates well with similar registration-based CT imaging methods and allows comparison of the local volume change and structural alterations, assessing structure–function relationships [117].

Pulmonary hypertension

Functional imaging has an established role in the assessment of patients with chronic thromboembolic pulmonary hypertension (CTEPH). Traditionally, planar ventilation and perfusion scintigraphy has been used in the evaluation and selection of patients for surgical pulmonary thromboendarterectomy or balloon angioplasty alongside right heart catheterisation, echocardiography and CT angiography [118]. DECT mapping of V_B allows the indirect detection of perfusion defects that appear as wedge-shaped areas of decreased blood volume, and has an incremental value in the diagnosis of acute pulmonary thromboembolism and CTEPH [119, 120], and may contribute to the differential diagnosis [121]. DECT has the advantage of revealing the detailed underlying lung morphology, large blood vessels and blood volume fraction at the voxel level.

A PET imaging study found that perfusion heterogeneity during NO inhalation can distinguish pulmonary arterial hypertension patients from healthy subjects and has potential as an imaging biomarker [51].

Lung cancer and preoperative assessment

Perhaps one of the earliest clinical applications of functional lung imaging has been the preoperative assessment of lung resection surgery candidates. Surgery is considered as the only curative therapy for many patients with lung cancer. Because resectable tumours often occur in patients with respiratory comorbidities, the current recommendations are to systematically assess lung function (FEV_1, D_{LCO}) prior to surgery [122]. An anatomic prediction of post-operative FEV_1 ($ppoFEV_1$) is based on preoperative FEV_1 and counting the number of segments to be removed. A $ppoFEV_1$ <30% is considered as the threshold to stratify high-risk patients [122]. In subjects with borderline lung function, functional imaging is recommended to predict post-operative lung function [122]. Both planar perfusion and ^{81m}Kr ventilation scintigraphy allow good prediction of $ppoFEV_1$, although perfusion scintigraphy with ^{99m}Tc-labelled macroaggregated albumin has been the most widely used method in patients undergoing pneumonectomy. However, planar scintigraphy may not be sufficiently accurate for predicting $ppoFEV_1$ after lobectomy [122]. In recent years, ventilation and perfusion DECT, SPECT, coregistered SPECT/CT, and dynamic contrast-enhanced MRI have been evaluated for predicting $ppoFEV_1$ in subjects with lung cancer [123]. Among these techniques, perfusion SPECT/CT and contrast-enhanced perfusion MRI have shown equivalent and better accuracy than planar scintigraphy in predicting post-operative lung function [124].

A common adverse complication induced by thoracic radiotherapy is radiation-induced lung injury (RILI), which manifests acutely as pneumonitis and chronically as fibrosis, significantly reducing patient survival and quality of life [125]. Increased incidental radiation dose to regions of high-functioning lung has exhibited correlation with increased radiation pneumonitis incidence [126]. Accordingly, the paradigm of functional lung avoidance radiotherapy (FLA-RT), where higher functioning lung regions, as defined by a functional lung imaging modality, are preferentially spared of radiation dose while maintaining tumour and other organ-at-risk dose constraints, may minimise RILI [127]. Several functional lung imaging modalities have been employed for FLA-RT; early studies investigated nuclear imaging-based SPECT *via* ^{99m}Tc-labelled macroaggregated albumin perfusion [128], while more recent nuclear imaging studies have employed PET *via* Gallium-68 ventilation and perfusion [129]. MRI-based FLA-RT studies have employed hyperpolarised ^{3}He MRI [130], with more recent work focussed on harnessing the unique properties of ^{129}Xe in terms of its moderate solubility in lung parenchyma and blood, facilitating gas exchange-guided

FLA-RT [131]. FLA-RT studies have also employed techniques developed to generate surrogates of regional ventilation from multi-inflation CT, acquired during tidal breathing or breath hold, without exogenous contrast or specialised equipment [132]. Such techniques are of particular interest to radiation oncology practitioners due to CT being routinely acquired as standard-of-care for thoracic oncology patients undergoing radiotherapy.

Research in physiology and pathophysiology

Pulmonary functional imaging studies in healthy subjects have revealed regional physiological characteristics in the lungs, including gradients, and their response to changes in external conditions. For example, the effect of prone and supine body positions on the topographical distribution of pulmonary perfusion and ventilation [133]. Additionally, pulmonary imaging studies have been invaluable in lung disease research yielding novel insights into regional disease processes and their dynamics, as demonstrated in this review. More accurate and technically challenging imaging methods may be primarily used in the research domain since robustness and cost are key constraints for clinical use. However, the findings of such imaging methods can nevertheless have far-reaching impacts on the clinical interpretation of common pulmonary function tests.

Conclusions

Several factors currently impede the more widespread clinical use of functional lung imaging. First, consensus on standardised definitions for image-derived lung functional metrics relying on basic physical and physiological principles is needed. Second, population-based normal reference values for key parameters are crucially required, as well as knowledge of the limits of normality and minimal clinically significant change. Finally, standardised protocols for quantitative reproducibility across imaging centres is a key step in improving the quality of future clinical trials. Another challenge is filling the evidence gap regarding the contribution of lung functional imaging to better patient outcomes. From a technical standpoint, image post-processing is often sophisticated, and fast and automated tools for processing and analysis are needed. Finally, robustness and cost-effectiveness remain significant challenges [4, 13, 134].

Despite these challenges, functional lung imaging has a number of strengths. It allows quantification of regional differences in lung function. It provides local information that traditional global lung function tests cannot access, and functional measurements that imaging techniques assessing anatomical structures are unable to perform. There is growing evidence that functional imaging allows sensitive detection of early-stage diseases, precise phenotyping of patient subtypes, provides surrogate biomarkers that can serve as intermediate end-points in drug or intervention trials, and gives valuable insight into the mechanisms of respiratory diseases. Ongoing technological developments aim at improving spatial, temporal and contrast sensitivity, and reduce or suppress ionising radiation. The most advanced and technically challenging methods may be primarily used in the research domain or for specific indications justifying the resources required beyond traditional testing methods.

Key points

- Pulmonary functional imaging using, for example, CT, MRI and nuclear imaging (SPECT, PET) can assess regional ventilation, perfusion, alveolar–capillary gas exchange, alveolar microstructure, biomechanical properties, and even cellular or molecular processes.
- Functional imaging allows local quantifications and assessments of regional differences, in contrast to the global averages of traditional lung function tests, and functional rather than the structural measurements that other imaging techniques yield.
- Functional imaging provides a unique insight into disease processes, early phase disease detection, precise lung functional phenotyping, and may provide imaging end-points for assessing new therapeutic interventions.
- Functional imaging is applied in major lung disorders, such as COPD, asthma, CF, interstitial lung diseases and pulmonary hypertension, as well as in preoperative assessment of lung resection.

Conflict of interest: T. Winkler reports support for the present manuscript from National Institutes of Health (NIH), USA, research grant R01HL141900. T. Winkler reports the following disclosures outside the submitted work: patents planned, issued or pending 1) US8527034B2 - Image derived input function for PET lung assessment, no royalty payments, and 2) DE 101 07 917 A 1 - Anordnung zur verbrauchsarmen Applikation gasförmiger Stoffe [Assembly for reducing consumption during the application of gaseous substances], no royalty payments. The remaining authors have nothing to disclose.

References

1 Woolcock AJ, Vincent N, Macklem PT. Frequency dependence of compliance as a test for obstruction in the small airways. *J Clin Invest* 1969; 48: 1097–1106.
2 Dyson NA, Hugh-Jones P, Newbery GR, *et al.* Studies of regional lung function using radioactive oxygen. *Br Med J* 1960; 1: 231–238.
3 West JB, Dollery CT. Distribution of blood flow and ventilation-perfusion ratio in the lung, measured with radioactive CO_2. *J Appl Physiol* 1960; 15: 405–410.
4 Gefter WB, Lee KS, Schiebler ML, *et al.* Pulmonary functional imaging: Part 2 – State-of-the-art clinical applications and opportunities for improved patient care. *Radiology* 2021; 299: 524–538.
5 Cala SJ, Kenyon CM, Ferrigno G, *et al.* Chest wall and lung volume estimation by optical reflectance motion analysis. *J Appl Physiol* 1996; 81: 2680–2689.
6 Marcucci C, Nyhan D, Simon BA. Distribution of pulmonary ventilation using Xe-enhanced computed tomography in prone and supine dogs. *J Appl Physiol* 2001; 90: 421–430.
7 Bayat S, Duc GL, Porra L, *et al.* Quantitative functional lung imaging with synchrotron radiation using inhaled xenon as contrast agent. *Phys Med Biol* 2001; 46: 3287–3299.
8 Bayat S, Dullin C, Kitchen MJ, *et al.* Synchrotron X-ray-based functional and anatomical lung imaging techniques. *In:* Giuliani A, Cedola A, eds. Advanced High-Resolution Tomography in Regenerative Medicine. Basel, Springer International Publishing, 2018; pp. 151–167.
9 Agostini A, Borgheresi A, Mari A, *et al.* Dual-energy CT: theoretical principles and clinical applications. *Radiol Med (Torino)* 2019; 124: 1281–1295.
10 Goo HW, Kim H, Goo JM. Basics and clinical application of CT for pulmonary functional evaluation. *In:* Ohno Y, Hatabu H, Kauczor HU, eds. Pulmonary Functional Imaging. Cham, Springer, 2021; pp. 21–45.
11 Ding K, Cao K, Fuld MK, *et al.* Comparison of image registration based measures of regional lung ventilation from dynamic spiral CT with Xe-CT. *Med Phys* 2012; 39: 5084–5098.
12 Galban CJ, Han MK, Boes JL, *et al.* Computed tomography-based biomarker provides unique signature for diagnosis of COPD phenotypes and disease progression. *Nat Med* 2012; 18: 1711–1715.
13 Woods JC, Wild JM, Wielpütz MO, *et al.* Current state of the art MRI for the longitudinal assessment of cystic fibrosis. *J Magn Reson Imaging* 2020; 52: 1306–1320.
14 Woodhouse N, Wild JM, Paley MN, *et al.* Combined helium-3/proton magnetic resonance imaging measurement of ventilated lung volumes in smokers compared to never-smokers. *J Magn Reson Imaging* 2005; 21: 365–369.
15 Ohno Y, Seo JB, Parraga G, *et al.* Pulmonary functional imaging: Part 1 – State-of-the-art technical and physiologic underpinnings. *Radiology* 2021; 299: 508–523.
16 Hughes PJ, Smith L, Chan H-F, *et al.* Assessment of the influence of lung inflation state on the quantitative parameters derived from hyperpolarized gas lung ventilation MRI in healthy volunteers. *J Appl Physiol* 2019; 126: 183–192.
17 Altes TA, Powers PL, Knight-Scott J, *et al.* Hyperpolarized ^{3}He MR lung ventilation imaging in asthmatics: preliminary findings. *J Magn Reson Imaging* 2001; 13: 378–384.
18 Wild JM, Paley MN, Kasuboski L, *et al.* Dynamic radial projection MRI of inhaled hyperpolarized ^{3}He gas. *Magn Reson Med* 2003; 49: 991–997.
19 Gutberlet M, Kaireit TF, Voskrebenzev A, *et al.* Free-breathing dynamic ^{19}F gas MR imaging for mapping of regional lung ventilation in patients with COPD. *Radiology* 2018; 286: 1040–1051.
20 Edelman RR, Hatabu H, Tadamura E, *et al.* Noninvasive assessment of regional ventilation in the human lung using oxygen–enhanced magnetic resonance imaging. *Nat Med* 1996; 2: 1236–1239.
21 Sa RC, Cronin MV, Henderson AC, *et al.* Vertical distribution of specific ventilation in normal supine humans measured by oxygen-enhanced proton MRI. *J Appl Physiol* 2010; 109: 1950–1959.
22 Alsop DC, Hatabu H, Bonnet M, *et al.* Multi-slice, breathhold imaging of the lung with submillisecond echo times. *Magn Reson Med* 1995; 33: 678–682.
23 Pennati F, Quirk JD, Yablonskiy DA, *et al.* Assessment of regional lung function with multivolume ^{1}H MR imaging in health and obstructive lung disease: comparison with ^{3}He MR imaging. *Radiology* 2014; 273: 580–590.
24 Mirza H, Hashmi MF. Lung Ventilation Perfusion Scan (VQ Scan). Treasure Island, StatPearls Publishing, 2023. www.ncbi.nlm.nih.gov/books/NBK564428/
25 Brudin LH, Rhodes CG, Valind SO, *et al.* Regional structure-function correlations in chronic obstructive lung disease measured with positron emission tomography. *Thorax* 1992; 47: 914–921.
26 Treppo S, Mijailovich SM, Venegas JG. Contributions of pulmonary perfusion and ventilation to heterogeneity in V_A/Q measured by PET. *J Appl Physiol* 1997; 82: 1163–1176.
27 Richard J-C, Janier M, Lavenne F, *et al.* Quantitative assessment of regional alveolar ventilation and gas volume using ^{13}N-N_2 washout and PET. *J Nucl Med* 2005; 46: 1375–1383.
28 Vidal Melo MF, Layfield D, Harris RS, *et al.* Quantification of regional ventilation-perfusion ratios with PET. *J Nucl Med* 2003; 44: 1982–1991.

29 Meier P, Zierler KL. On the theory of the indicator-dilution method for measurement of blood flow and volume. *J Appl Physiol* 1954; 6: 731–744.
30 Fuld MK, Halaweish AF, Haynes SE, *et al.* Pulmonary perfused blood volume with dual-energy CT as surrogate for pulmonary perfusion assessed with dynamic multidetector CT. *Radiology* 2013; 267: 747–756.
31 Schuster DP, Anderson C, Kozlowski J, *et al.* Regional pulmonary perfusion in patients with acute pulmonary edema. *J Nucl Med* 2002; 43: 863–870.
32 Johns CS, Swift AJ, Hughes PJC, *et al.* Pulmonary MR angiography and perfusion imaging – a review of methods and applications. *Eur J Radiol* 2017; 86: 361–370.
33 Levine D, McDonald RJ, Kressel HY. Gadolinium retention after contrast-enhanced MRI. *JAMA* 2018; 320: 1853–1854.
34 Taso M, Aramendía-Vidaurreta V, Englund EK, *et al.* Update on state-of-the-art for arterial spin labeling (ASL) human perfusion imaging outside of the brain. *Magn Reson Med* 2023; 89: 1754–1776.
35 Hopkins SR. Ventilation/perfusion relationships and gas exchange: measurement approaches. *Compr Physiol* 2020; 10: 1155.
36 Voskrebenzev A, Gutberlet M, Klimeš F, *et al.* Feasibility of quantitative regional ventilation and perfusion mapping with phase-resolved functional lung (PREFUL) MRI in healthy volunteers and COPD, CTEPH, and CF patients. *Magn Reson Med* 2018; 79: 2306–2314.
37 François CJ, Srinivasan S, Schiebler ML, *et al.* 4D cardiovascular magnetic resonance velocity mapping of alterations of right heart flow patterns and main pulmonary artery hemodynamics in tetralogy of Fallot. *J Cardiovasc Magn Reson* 2012; 14: 16.
38 Lovering AT, Haverkamp HC, Romer LM, *et al.* Transpulmonary passage of ^{99m}Tc macroaggregated albumin in healthy humans at rest and during maximal exercise. *J Appl Physiol* 2009; 106: 1986–1992.
39 Vidal Melo MF, Harris RS, Layfield JDH, *et al.* Topographic basis of bimodal ventilation-perfusion distributions during bronchoconstriction in sheep. *Am J Respir Crit Care Med* 2005; 171: 714–721.
40 Winkler T, Melo MFV, Degani-Costa LH, *et al.* Estimation of noise-free variance to measure heterogeneity. *PLoS One* 2015; 10: e0123417.
41 Vidal Melo MF, Winkler T, Harris RS, *et al.* Spatial heterogeneity of lung perfusion assessed with ^{13}N PET as a vascular biomarker in chronic obstructive pulmonary disease. *J Nucl Med* 2010; 51: 57–65.
42 Kohli P, Kelly VJ, Kehl EG, *et al.* Perfusion imaging distinguishes exercise pulmonary arterial hypertension at rest. *Am J Respir Crit Care Med* 2019; 199: 1438–1441.
43 Schuster DP, Kaplan JD, Gauvain K, *et al.* Measurement of regional pulmonary blood flow with PET. *J Nucl Med* 1995; 36: 371–377.
44 Wagner PD. The multiple inert gas elimination technique (MIGET). *Intensive Care Med* 2008; 34: 994–1001.
45 Brudin LH, Rhodes CG, Valind SO, *et al.* Relationships between regional ventilation and vascular and extravascular volume in supine humans. *J Appl Physiol* 1994; 76: 1195–1204.
46 Sá RC, Henderson AC, Simonson T, *et al.* Measurement of the distribution of ventilation-perfusion ratios in the human lung with proton MRI: comparison with the multiple inert-gas elimination technique. *J Appl Physiol* 2017; 123: 136–146.
47 Kelly VJ, Hibbert KA, Kohli P, *et al.* Hypoxic pulmonary vasoconstriction does not explain all regional perfusion redistribution in asthma. *Am J Respir Crit Care Med* 2017; 196: 834–844.
48 Kelly VJ, Winkler T, Harris RS. Reply to Dorrington, *et al*. and to Swenson: “Hypercapnic pulmonary vasoconstriction contributes to regional perfusion distribution: relevance to asthma” and “Hypercapnic pulmonary vasoconstriction as a mechanism for regional perfusion redistribution in asthma”. *Am J Respir Crit Care Med* 2018; 197: 684.
49 Johansen T, Winkler T, Kelly VJ, *et al.* A method for mapping regional oxygen and CO_2 transfer in the lung. *Respir Physiol Neurobiol* 2016; 222: 29–47.
50 Beda A, Winkler T, Wellman TJ, *et al.* Physiological mechanism and spatial distribution of increased alveolar dead-space in early ARDS: an experimental study. *Acta Anaesthesiol Scand* 2021; 65: 100–108.
51 Winkler T, Kohli P, Kelly VJ, *et al.* Perfusion imaging heterogeneity during NO inhalation distinguishes pulmonary arterial hypertension (PAH) from healthy subjects and has potential as an imaging biomarker. *Respir Res* 2022; 23: 325.
52 Wagner PD, Hedenstierna G, Bylin G, *et al.* Reproducibility of the multiple inert gas elimination technique. *J Appl Physiol* 1987; 62: 1740–1746.
53 Wagner PD, Hedenstierna G, Bylin G. Ventilation–perfusion inequality in chronic asthma. *Am Rev Respir Dis* 1987; 136: 605–612.
54 Patz S, Muradian I, Hrovat MI, *et al.* Human pulmonary imaging and spectroscopy with hyperpolarized ^{129}Xe at 0.2T. *Acad Radiol* 2008; 15: 713–727.
55 Stewart NJ, Leung G, Norquay G, *et al.* Experimental validation of the hyperpolarized ^{129}Xe chemical shift saturation recovery technique in healthy volunteers and subjects with interstitial lung disease. *Magn Reson Med* 2015; 74: 196–207.

56 Wang JM, Robertson SH, Wang Z, *et al.* Using hyperpolarized ^{129}Xe MRI to quantify regional gas transfer in idiopathic pulmonary fibrosis. *Thorax* 2018; 73: 21–28.
57 Weatherley ND, Stewart NJ, Chan H-F, *et al.* Hyperpolarised xenon magnetic resonance spectroscopy for the longitudinal assessment of changes in gas diffusion in IPF. *Thorax* 2019; 74: 500–502.
58 Hahn AD, Carey KJ, Barton GP, *et al.* Hyperpolarized ^{129}Xe MR spectroscopy in the lung shows 1-year reduced function in idiopathic pulmonary fibrosis. *Radiology* 2022; 305: 688–696.
59 Saunders LC, Collier GJ, Chan H-F, *et al.* Longitudinal lung function assessment of patients hospitalised with COVID-19 using ^{1}H and ^{129}Xe lung MRI. *Chest* 2023; 164: 700–716.
60 Kaplan JD, Trulock EP, Anderson DJ, *et al.* Pulmonary vascular permeability in interstitial lung disease: a positron emission tomographic study. *Am Rev Respir Dis* 1992; 145: 1495–1498.
61 Bhatt SP, Bodduluri S, Hoffman EA, *et al.* Computed tomography measure of lung at risk and lung function decline in chronic obstructive pulmonary disease. *Am J Respir Crit Care Med* 2017; 196: 569–576.
62 Cercos-Pita J-L, Fardin L, Leclerc H, *et al.* Lung tissue biomechanics imaged with synchrotron phase contrast microtomography in live rats. *Sci Rep* 2021; 12: 5056.
63 Marinelli JP, Levin DL, Vassallo R, *et al.* Quantitative assessment of lung stiffness in patients with interstitial lung disease using MR elastography. *J Magn Reson Imaging* 2017; 46: 365–374.
64 Miravitlles M, Soler-Cataluña JJ, Calle M, *et al.* Treatment of COPD by clinical phenotypes: putting old evidence into clinical practice. *Eur Respir J* 2013; 41: 1252–1256.
65 Martinez FJ, Han MK, Allinson JP, *et al.* At the root: defining and halting progression of early chronic obstructive pulmonary disease. *Am J Respir Crit Care Med* 2018; 197: 1540–1551.
66 Bhatt SP, Bodduluri S, Newell JD, *et al.* CT-derived biomechanical metrics improve agreement between spirometry and emphysema. *Acad Radiol* 2016; 23: 1255–1263.
67 Boes JL, Hoff BA, Bule M, *et al.* Parametric response mapping monitors temporal changes on lung CT scans in the subpopulations and intermediate outcome measures in COPD Study (SPIROMICS). *Acad Radiol* 2015; 22: 186–194.
68 Cohen J, Shekarnabi M, Destors M, *et al.* Computed tomography registration-derived regional ventilation indices compared to global lung function parameters in patients with COPD. *Front Physiol* 2022; 13: 862186.
69 Alford SK, van Beek EJ, McLennan G, *et al.* Heterogeneity of pulmonary perfusion as a mechanistic image-based phenotype in emphysema susceptible smokers. *Proc Natl Acad Sci USA* 2010; 107: 7485–7490.
70 Park E-A, Goo JM, Park SJ, *et al.* Chronic obstructive pulmonary disease: quantitative and visual ventilation pattern analysis at xenon ventilation CT performed by using a dual-energy technique. *Radiology* 2010; 256: 985–997.
71 Swift AJ, Wild JM, Fichele S, *et al.* Emphysematous changes and normal variation in smokers and COPD patients using diffusion ^{3}He MRI. *Eur J Radiol* 2005; 54: 352–358.
72 Fain SB, Panth SR, Evans MD, *et al.* Early emphysematous changes in asymptomatic smokers: detection with ^{3}He MR imaging. *Radiology* 2006; 239: 875–883.
73 MacNeil JL, Capaldi DP, Westcott AR, *et al.* Pulmonary imaging phenotypes of chronic obstructive pulmonary disease using multiparametric response maps. *Radiology* 2020; 295: 227–236.
74 Marshall H, Deppe MH, Parra-Robles J, *et al.* Direct visualisation of collateral ventilation in COPD with hyperpolarised gas MRI. *Thorax* 2012; 67: 613–617.
75 Myc L, Qing K, He M, *et al.* Characterisation of gas exchange in COPD with dissolved-phase hyperpolarised xenon-129 MRI. *Thorax* 2021; 76: 178–181.
76 Kohli P, Kelly VJ, Hibbert KA, *et al.* PET imaging reveals early pulmonary perfusion abnormalities in HIV infection similar to smoking. *J Nucl Med* 2021; 62: 405–411.
77 Singh D, Wild JM, Saralaya D, *et al.* Effect of indacaterol/glycopyrronium on ventilation and perfusion in COPD: a randomized trial. *Respir Res* 2022; 23: 26.
78 Vogel-Claussen J, Schönfeld C-O, Kaireit TF, *et al.* Effect of indacaterol/glycopyrronium on pulmonary perfusion and ventilation in hyperinflated patients with chronic obstructive pulmonary disease (CLAIM). A double-blind, randomized, crossover trial. *Am J Respir Crit Care Med* 2019; 199: 1086–1096.
79 King GG, Farrow CE, Chapman DG. Dismantling the pathophysiology of asthma using imaging. *Eur Respir Rev* 2019; 28: 180111.
80 Dunican EM, Elicker BM, Henry T, *et al.* Mucus plugs and emphysema in the pathophysiology of airflow obstruction and hypoxemia in smokers. *Am J Respir Crit Care Med* 2021; 203: 957–968.
81 Okazawa M, Müller N, McNamara AE, *et al.* Human airway narrowing measured using high resolution computed tomography. *Am J Respir Crit Care Med* 1996; 154: 1557–1562.
82 King GG, Carroll JD, Müller NL, *et al.* Heterogeneity of narrowing in normal and asthmatic airways measured by HRCT. *Eur Respir J* 2004; 24: 211–218.
83 Dame Carroll JR, Magnussen JS, Berend N, *et al.* Greater parallel heterogeneity of airway narrowing and airway closure in asthma measured by high-resolution CT. *Thorax* 2015; 70: 1163–1170.
84 Verbanck S, Schuermans D, Noppen M, *et al.* Evidence of acinar airway involvement in asthma. *Am J Respir Crit Care Med* 1999; 159: 1545–1550.

85 Bentivoglio LG, Beerel F, Bryan AC, *et al.* Regional pulmonary function studied with xenon in patients with bronchial asthma. *J Clin Invest* 1963; 42: 1193–1200.

86 Farrow CE, Salome CM, Harris BE, *et al.* Peripheral ventilation heterogeneity determines the extent of bronchoconstriction in asthma. *J Appl Physiol* 2017; 123: 1188–1194.

87 Venegas JG, Winkler T, Musch G, *et al.* Self-organized patchiness in asthma as a prelude to catastrophic shifts. *Nature* 2005; 434: 777–782.

88 Winkler T, Venegas JG. Complex airway behavior and paradoxical responses to bronchoprovocation. *J Appl Physiol* 2007; 103: 655–663.

89 Winkler T, Frey U. Airway remodeling: shifting the trigger point for exacerbations in asthma. *J Allergy Clin Immunol* 2021; 148: 710–712.

90 Krings JG, Goss CW, Lew D, *et al.* Quantitative CT metrics are associated with longitudinal lung function decline and future asthma exacerbations: results from SARP-3. *J Allergy Clin Immunol* 2021; 148: 752–762.

91 Greenblatt EE, Winkler T, Harris RS, *et al.* What causes uneven aerosol deposition in the bronchoconstricted lung? A quantitative imaging study. *J Aerosol Med Pulm Drug Deliv* 2016; 29: 57–75.

92 Sovijarvi AR, Poyhonen L, Kellomaki L, *et al.* Effects of acute and long-term bronchodilator treatment on regional lung function in asthma assessed with krypton-81m and technetium-99m-labelled macroaggregates. *Thorax* 1982; 37: 516–520.

93 Harris RS, Winkler T, Tgavalekos N, *et al.* Regional pulmonary perfusion, inflation, and ventilation defects in bronchoconstricted patients with asthma. *Am J Respir Crit Care Med* 2006; 174: 245–253.

94 Lin NY, Roach DJ, Willmering MM, *et al.* ^{129}Xe MRI as a measure of clinical disease severity for pediatric asthma. *J Allergy Clin Immunol* 2021; 147: 2146–2153.

95 Horn FC, Marshall H, Collier GJ, *et al.* Regional ventilation changes in the lung: treatment response mapping by using hyperpolarized gas MR imaging as a quantitative biomarker. *Radiology* 2017; 284: 854–861.

96 Svenningsen S, Eddy RL, Kjarsgaard M, *et al.* Effects of anti-T2 biologic treatment on lung ventilation evaluated by MRI in adults with prednisone-dependent asthma. *Chest* 2020; 158: 1350–1360.

97 Hall CS, Quirk JD, Goss CW, *et al.* Single-session bronchial thermoplasty guided by ^{129}Xe magnetic resonance imaging. A pilot randomized controlled clinical trial. *Am J Respir Crit Care Med* 2020; 202: 524–534.

98 Eddy RL, McIntosh MJ, Matheson AM, *et al.* Pulmonary MRI and cluster analysis help identify novel asthma phenotypes. *J Magn Reson Imaging* 2022; 56: 1475–1486.

99 Chae EJ, Seo JB, Lee J, *et al.* Xenon ventilation imaging using dual-energy computed tomography in asthmatics: initial experience. *Invest Radiol* 2010; 45: 354–361.

100 Raghu G, Richeldi L, Jagerschmidt A, *et al.* Idiopathic pulmonary fibrosis: prospective, case-controlled study of natural history and circulating biomarkers. *Chest* 2018; 154: 1359–1370.

101 Scharm SC, Vogel-Claussen J, Schaefer-Prokop C, *et al.* Quantification of dual-energy CT-derived functional parameters as potential imaging markers for progression of idiopathic pulmonary fibrosis. *Eur Radiol* 2021; 31: 6640–6651.

102 Chassagnon G, Martin C, Marini R, *et al.* Use of elastic registration in pulmonary MRI for the assessment of pulmonary fibrosis in patients with systemic sclerosis. *Radiology* 2019; 291: 487–492.

103 Wang Z, Robertson SH, Wang J, *et al.* Quantitative analysis of hyperpolarized ^{129}Xe gas transfer MRI. *Med Phys* 2017; 44: 2415–2428.

104 Montesi SB, Zhou IY, Liang LL, *et al.* Dynamic contrast-enhanced magnetic resonance imaging of the lung reveals important pathobiology in idiopathic pulmonary fibrosis. *ERJ Open Res* 2021; 7: 00907-2020.

105 Weatherley ND, Eaden JA, Hughes PJC, *et al.* Quantification of pulmonary perfusion in idiopathic pulmonary fibrosis with first pass dynamic contrast-enhanced perfusion MRI. *Thorax* 2021; 76: 144–151.

106 Chen DL, Ballout S, Chen L, *et al.* Consensus recommendations on the use of ^{18}F-FDG PET/CT in lung disease. *J Nucl Med* 2020; 61: 1701–1707.

107 Jordon L, Ganeshan B, Nadeem I, *et al.* Can FDG-PET/CT imaging be used to prognosticate in interstitial lung disease? A prospective study of the relationship between FDG-PET/CT measurements and quality of life. *Eur Respir J* 2022; 60: Suppl. 66, 2473.

108 Liang J, Cao H, Liu Y, *et al.* The lungs were on fire: a pilot study of ^{18}F-FDG PET/CT in idiopathic-inflammatory-myopathy-related interstitial lung disease. *Arthritis Res Ther* 2021; 23: 198.

109 Spielberg DR, Clancy JP. Cystic fibrosis and its management through established and emerging therapies. *Annu Rev Genomics Hum Genet* 2016; 17: 155–175.

110 Ciet P, Bertolo S, Ros M, *et al.* State-of-the-art review of lung imaging in cystic fibrosis with recommendations for pulmonologists and radiologists from the "iMAging managEment of cySTic fibROsis" (MAESTRO) consortium. *Eur Respir Rev* 2022; 31: 210173.

111 Brody AS, Klein JS, Molina PL, *et al.* High-resolution computed tomography in young patients with cystic fibrosis: distribution of abnormalities and correlation with pulmonary function tests. *J Pediatr* 2004; 145: 32–38.

112 Marshall H, Horsley A, Taylor CJ, *et al.* Detection of early subclinical lung disease in children with cystic fibrosis by lung ventilation imaging with hyperpolarised gas MRI. *Thorax* 2017; 72: 760–762.

113 Kanhere N, Couch MJ, Kowalik K, *et al.* Correlation of lung clearance index with hyperpolarized ^{129}Xe magnetic resonance imaging in pediatric subjects with cystic fibrosis. *Am J Respir Crit Care Med* 2017; 196: 1073–1075.

114 Altes TA, Johnson M, Fidler M, *et al.* Use of hyperpolarized helium-3 MRI to assess response to ivacaftor treatment in patients with cystic fibrosis. *J Cyst Fibros* 2017; 16: 267–274.

115 Wielpütz MO, Puderbach M, Kopp-Schneider A, *et al.* Magnetic resonance imaging detects changes in structure and perfusion, and response to therapy in early cystic fibrosis lung disease. *Am J Respir Crit Care Med* 2014; 189: 956–965.

116 Nyilas S, Bauman G, Sommer G, *et al.* Novel magnetic resonance technique for functional imaging of cystic fibrosis lung disease. *Eur Respir J* 2017; 50: 1701464.

117 Pennati F, Roach DJ, Clancy JP, *et al.* Assessment of pulmonary structure–function relationships in young children and adolescents with cystic fibrosis by multivolume proton-MRI and CT. *J Magn Reson Imaging* 2018; 48: 531–542.

118 Gefter WB. Functional CT imaging of the lungs. *Acad Radiol* 2002; 9: 127–129.

119 Le Faivre J, Duhamel A, Khung S, *et al.* Impact of CT perfusion imaging on the assessment of peripheral chronic pulmonary thromboembolism: clinical experience in 62 patients. *Eur Radiol* 2016; 26: 4011–4020.

120 Hong YJ, Kim JY, Choe KO, *et al.* Different perfusion pattern between acute and chronic pulmonary thromboembolism: evaluation with two-phase dual-energy perfusion CT. *Am J Roentgenol* 2013; 200: 812–817.

121 Renapurkar RD, Shrikanthan S, Heresi GA, *et al.* Imaging in chronic thromboembolic pulmonary hypertension. *J Thorac Imaging* 2017; 32: 71–88.

122 Brunelli A, Charloux A, Bolliger C, *et al.* ERS/ESTS clinical guidelines on fitness for radical therapy in lung cancer patients (surgery and chemo-radiotherapy). *Eur Respir J* 2009; 34: 17–41.

123 Ohno Y, Koyama H, Murayama K, *et al.* Functional assessment of lung cancer and nodules. *In:* Ohno Y, Hatabu H, Kauczor HU, eds. Pulmonary Functional Imaging. Cham, Springer, 2021; pp. 259–297.

124 Ohno Y, Koyama H, Nogami M, *et al.* State-of-the-art radiological techniques improve the assessment of postoperative lung function in patients with non-small cell lung cancer. *Eur J Radiol* 2011; 77: 97–104.

125 Palma DA, Senan S, Tsujino K, *et al.* Predicting radiation pneumonitis after chemoradiation therapy for lung cancer: an international individual patient data meta-analysis. *Int J Radiat Oncol Biol Phys* 2013; 85: 444–450.

126 Faught AM, Yamamoto T, Castillo R, *et al.* Evaluating which dose-function metrics are most critical for functional-guided radiation therapy. *Int J Radiat Oncol Biol Phys* 2017; 99: 202–209.

127 Ireland RH, Tahir BA, Wild JM, *et al.* Functional image-guided radiotherapy planning for normal lung avoidance. *Clin Oncol* 2016; 28: 695–707.

128 Munawar I, Yaremko BP, Craig J, *et al.* Intensity modulated radiotherapy of non-small-cell lung cancer incorporating SPECT ventilation imaging. *Med Phys* 2010; 37: 1863–1872.

129 Bucknell NW, Hardcastle N, Bressel M, *et al.* Functional lung imaging in radiation therapy for lung cancer: a systematic review and meta-analysis. *Radiother Oncol* 2018; 129: 196–208.

130 Tahir BA, Bragg CM, Wild JM, *et al.* Impact of field number and beam angle on functional image-guided lung cancer radiotherapy planning. *Phys Med Biol* 2017; 62: 7114–7130.

131 Rankine LJ, Wang Z, Kelsey CR, *et al.* Hyperpolarized ^{129}Xe magnetic resonance imaging for functional avoidance treatment planning in thoracic radiation therapy: a comparison of ventilation- and gas exchange-guided treatment plans. *Int J Radiat Oncol Biol Phys* 2021; 111: 1044–1057.

132 Yamamoto T, Kabus S, Bal M, *et al.* The first patient treatment of computed tomography ventilation functional image-guided radiotherapy for lung cancer. *Radiother Oncol* 2016; 118: 227–231.

133 Musch G, Layfield JDH, Harris RS, *et al.* Topographical distribution of pulmonary perfusion and ventilation, assessed by PET in supine and prone humans. *J Appl Physiol* 2002; 93: 1841–1851.

134 Ohno Y, Hatabu H. Future of pulmonary functional imaging. *In*: Ohno Y, Hatabu H, Kauczor HU, eds. Pulmonary Functional Imaging. Cham, Springer, 2021; pp. 337–360.

135 Harris RS, Winkler T, Musch G, *et al.* The prone position results in smaller ventilation defects during bronchoconstriction in asthma. *J Appl Physiol* 2009; 107: 266–274.